

# Preconditioning Compressible Flow Calculations on Stretched Meshes

*Niles A. Pierce\** and *Michael B. Giles†*

Oxford University Computing Laboratory  
Numerical Analysis Group  
Oxford OX1 3QD, UK

## Abstract

High aspect ratio cells in a computational mesh compound the inherent stiffness in the Euler and Navier–Stokes equations which arises from a disparity in the propagative speeds of convective and acoustic modes. A mesh-aligned preconditioning strategy is examined which improves full coarsening multigrid performance by clustering high frequency components of the spatial Fourier footprint away from the origin for effective damping by a Runge-Kutta time stepping scheme. For viscous computations on highly stretched meshes, a J-coarsening multigrid algorithm is adopted that provides adequate clustering of all modes inside the boundary layer. In contrast to previous approaches, the methods presented are robust when used in conjunction with high resolution schemes on fine meshes and with multigrid. Substantial speed-ups are demonstrated for a variety of Euler and laminar and turbulent Navier-Stokes test cases.

## 1 Introduction

Explicit Euler and Navier–Stokes solvers based on multigrid remain popular due to ease of programming and suitability for parallelization despite the fact that convergence is significantly hampered by the use of a scalar time step limit which is appropriate only for the fastest propagating mode. This deficiency is most apparent in the stretched boundary layer cells of a viscous mesh, where the CFL condition produces an explicit scalar time step based on the transverse acoustic mode  $\Delta t = O(\Delta y/c)$ . This time step is typically several

orders of magnitude more restrictive than necessary for the streamwise and transverse convective modes, for which a more appropriate constraint is  $\Delta t = O(\Delta x/u) = O(\Delta y/v)$ . Motivated by the resulting breakdown of multigrid convergence in highly stretched boundary layer cells, Allmaras proposed the use of an implicit ADI preconditioner for full coarsening multigrid and preconditioners based on point-implicit block-Jacobi and semi-implicit line-Jacobi for the semi-coarsening multigrid algorithm of Mulder [1, 2, 14, 15].

These suggestions are motivated by the realization that for efficient multigrid performance, the relaxation scheme on each mesh must damp all modes which cannot be resolved without aliasing on the next coarser mesh in the cycle. Preconditioning is intended to cluster the residual eigenvalues of these unresolvable modes away from the origin in Fourier space so that they can be rapidly damped by a multi-stage time stepping scheme. Using full coarsening multigrid in 2D, only modes which are low frequency in both mesh directions can be resolved on the coarser grids, so the relaxation scheme must damp all high frequency modes and also those modes that are high frequency in one mesh direction and low frequency in the other. Allmaras recommends an implicit preconditioner because explicit methods are notoriously poor at damping modes with a low frequency component [2].

Alternatively, the semi-coarsening algorithm proposed by Mulder [14, 15] coarsens separately in each mesh direction and therefore reduces the region of Fourier space for which the relaxation scheme on each mesh must successfully damp modes for the algorithm to function efficiently. To obtain an  $O(N)$  method for a 3D mesh with  $N$  points, Mulder defined a restriction and prolongation structure in which not all grids are coarsened in every direction. For 2D grids that are coarsened separately in both direc-

\* Doctoral Candidate, Student Member AIAA

† Rolls Royce Reader in CFD, Member AIAA

Copyright ©1996 by the American Institute of Aeronautics and Astronautics, Inc. All rights reserved.

tions, only those modes which are high frequency in both mesh directions need be damped by the relaxation scheme. For this purpose, Allmaras suggests a point-implicit block-Jacobi preconditioner that has previously been demonstrated to be effective in clustering high frequency eigenvalues away from the origin [1]. For grids that are not coarsened in one of the mesh directions, Allmaras proposes using a semi-implicit line-Jacobi preconditioner in that direction [2].

These strategies for preconditioning in the context of both full and semi-coarsening multigrid are well-conceived. The drawback to implicit preconditioning for full coarsening multigrid is the increased complexity in developing parallel implementations. The drawback to a semi-coarsening approach is that for a 3D computation, the cost of a full coarsening W-cycle is bounded by  $\frac{4}{3}N$ , while a semi-coarsening W-cycle is no longer  $O(N)$  and the bounds for V and F-cycles are  $8N$  and  $32N$ , respectively [9, 14].

The present work explores the possibility of developing an effective strategy for stretched mesh computations that combines the simplicity of point-implicit block-Jacobi preconditioning with the low cost of full coarsening multigrid or a reduced semi-coarsening algorithm. Analytic expressions for the preconditioned Fourier footprints are obtained for six important asymptotic limits of flow and cell variables, including two cases for the full Navier–Stokes equations. Clustering behavior is examined for high frequency modes and the implications for modes with a low frequency component in one mesh direction are also considered. Emphasis is placed on demonstrating viability for practical aerodynamic computations including turbulent flows.

## 2 Approach

A preconditioned semi-discrete finite volume scheme appears as

$$\frac{dW_{i,k}}{dt} + PR(W) = 0, \quad (1)$$

where  $R(W)$  is the residual vector of the spatial discretization and  $P$  is a local preconditioner designed to reduce stiffness arising from variation in the flow and mesh parameters. The form of the preconditioner is based on the linearized 2D Navier–Stokes equations in Cartesian coordinates

$$\frac{\partial W}{\partial t} + A \frac{\partial W}{\partial x} + B \frac{\partial W}{\partial y} = C \frac{\partial^2 W}{\partial x^2} + D \frac{\partial^2 W}{\partial y^2} + E \frac{\partial^2 W}{\partial x \partial y},$$

from which the Euler equations may be obtained by eliminating the viscous terms on the right hand side. A Cartesian mesh is assumed to simplify notation,

but the theory extends naturally to a  $(\xi, \eta)$  mesh-aligned coordinate system for real applications.

### 2.1 Scalar Preconditioner

A conservative time step estimate for the Navier–Stokes equations is based on the purely hyperbolic and parabolic time steps formed using the spectral radii of the flux Jacobians [13],

$$\Delta t_{NS}^{-1} = \Delta t_H^{-1} + \Delta t_P^{-1},$$

where the hyperbolic time step is given by

$$\Delta t_H^{-1} = \frac{1}{\text{CFL}_H} \left( \frac{\rho(A)}{\Delta x} + \frac{\rho(B)}{\Delta y} \right)$$

and the parabolic time step is

$$\Delta t_P^{-1} = \frac{1}{\text{CFL}_P} \left( \frac{4\rho(C)}{\Delta x^2} + \frac{4\rho(D)}{\Delta y^2} + \frac{\rho(E)}{\Delta x \Delta y} \right).$$

The factor of 4 in the parabolic time step arises from considering the worst-case scenario of a checkerboard mode,  $W_{j,k} = \widehat{W}(t)e^{i(\pi j + \pi k)}$ , for which the coefficients of the 2nd difference stencil reinforce each other in both directions. The hyperbolic and parabolic CFL numbers,  $\text{CFL}_H$  and  $\text{CFL}_P$ , reflect the extent of the multi-stage time stepping scheme stability region along the imaginary and negative real axes, respectively. On a real computational mesh in which  $\Delta x$  and  $\Delta y$  vary, this time step limit defines a suitable scalar preconditioner for the Navier–Stokes equations,  $P_{NS}^{-1} = \Delta t_{NS}^{-1}$ , that reduces stiffness resulting from variation in spectral radius and minimum cell dimension throughout the mesh.

For the Euler equations, the corresponding scalar preconditioner is defined by the purely hyperbolic time step,  $P_{SE}^{-1} = \Delta t_H^{-1}$ , assuming that the numerical dissipation introduced to prevent decoupling is sufficiently small so as not to limit the stability. The implications of this assumption for the scaling of the numerical dissipation are examined more thoroughly in reference [16].

### 2.2 Block-Jacobi Preconditioner

The block-Jacobi preconditioner is based on the specific structure of the discrete residual vector. For a preconditioned semi-discrete scheme of the form (1), the residual for a standard spatial discretization incorporating a 2nd/4th difference switch of the type introduced by Jameson *et al.* [11] applied to Roe–

averaged characteristic variables [17], takes the form

$$\begin{aligned}
R &= \frac{A}{2\Delta x} \delta_{2x} - (S_x) \frac{|A|}{2\Delta x} \delta_{xx} + (1 - S_x) \varepsilon^{(4)} \frac{|A|}{\Delta x} \delta_{xxxx} \\
&+ \frac{B}{2\Delta y} \delta_{2y} - (S_y) \frac{|B|}{2\Delta y} \delta_{yy} + (1 - S_y) \varepsilon^{(4)} \frac{|B|}{\Delta y} \delta_{yyyy} \\
&- \frac{C}{\Delta x^2} \delta_{xx} - \frac{D}{\Delta y^2} \delta_{yy} - \frac{E}{4\Delta x \Delta y} \delta_{2x2y},
\end{aligned} \tag{2}$$

where  $S$  is a switch taking values between zero and one.

The block-Jacobi preconditioner is obtained by extracting the elements of the residual operator which correspond to the central node

$$\begin{aligned}
P_{J_{NS}}^{-1} &= \frac{1}{\text{CFLH}} \left\{ [S_x + 6\varepsilon^{(4)}(1 - S_x)] \frac{|A|}{\Delta x} \right. \\
&\quad + [S_y + 6\varepsilon^{(4)}(1 - S_y)] \frac{|B|}{\Delta y} \\
&\quad \left. + \frac{2C}{\Delta x^2} + \frac{2D}{\Delta y^2} \right\}.
\end{aligned}$$

From this expression it is apparent that for a 4th difference dissipation coefficient of  $\varepsilon^{(4)} = \frac{1}{6}$ , the block-Jacobi preconditioner is identical for both 2nd and 4th differences. This value is adopted to simplify analysis and is found in practice to be a very suitable coefficient for matrix characteristic-based dissipation, though it would be far too dissipative for a scalar scheme. The simplified block-Jacobi preconditioner for the 2D Navier–Stokes equations may therefore be written

$$P_{J_{NS}}^{-1} = \frac{1}{\text{CFLH}} \left( \frac{|A|}{\Delta x} + \frac{|B|}{\Delta y} + \frac{2C}{\Delta x^2} + \frac{2D}{\Delta y^2} \right).$$

In this form it is equally suitable for both smooth and shocked regions of the flow, where the two different types of numerical dissipation are active. The block-Jacobi preconditioner for the 2D Euler equations is obtained by eliminating the viscous terms

$$P_{J_E}^{-1} = \frac{1}{\text{CFLH}} \left( \frac{|A|}{\Delta x} + \frac{|B|}{\Delta y} \right).$$

From these definitions, it is evident that block-Jacobi preconditioners must be used in conjunction with matrix dissipation, since they reduce to scalar preconditioners by identity using standard scalar dissipation based on the spectral radii of the flux Jacobians.

## 3 Analysis

### 3.1 Fourier Footprints

In the context of a semi-discrete scheme (1), the Fourier footprint of the spatial discretization is critical in determining the effectiveness of a multi-stage

time stepping scheme in damping error modes. The footprint is found by substituting a semi-discrete Fourier mode of the form

$$W_{j,k} = \widehat{W}(t) e^{i(j\theta_x + k\theta_y)}$$

into the discrete residual operator (2). The Fourier amplitude  $\widehat{W}(t)$  satisfies the evolution equation

$$\frac{d\widehat{W}}{dt} + PZ\widehat{W} = 0,$$

where  $Z$  is the Fourier symbol of the residual operator

$$\begin{aligned}
Z(\theta_x, \theta_y) &= i \frac{A}{\Delta x} \sin \theta_x + (S_x) \frac{|A|}{\Delta x} (1 - \cos \theta_x) \\
&+ (1 - S_x) 4\varepsilon^{(4)} \frac{|A|}{\Delta x} (1 - \cos \theta_x)^2 \\
&+ i \frac{B}{\Delta y} \sin \theta_y + (S_y) \frac{|B|}{\Delta y} (1 - \cos \theta_y) \\
&+ (1 - S_y) 4\varepsilon^{(4)} \frac{|B|}{\Delta y} (1 - \cos \theta_y)^2 \\
&+ \frac{2C}{\Delta x^2} (1 - \cos \theta_x) + \frac{2D}{\Delta y^2} (1 - \cos \theta_y) \\
&+ \frac{E}{\Delta x \Delta y} \sin \theta_x \sin \theta_y.
\end{aligned}$$

The Fourier footprint is obtained numerically by computing the eigenvalues of  $PZ$  for the desired range of the Fourier angles  $(\theta_x, \theta_y)$ . For stability, the footprint must lie within the stability region of the time stepping scheme defined by  $|\psi(z)| \leq 1$ , where  $\psi(z)$  is the amplification factor defined by

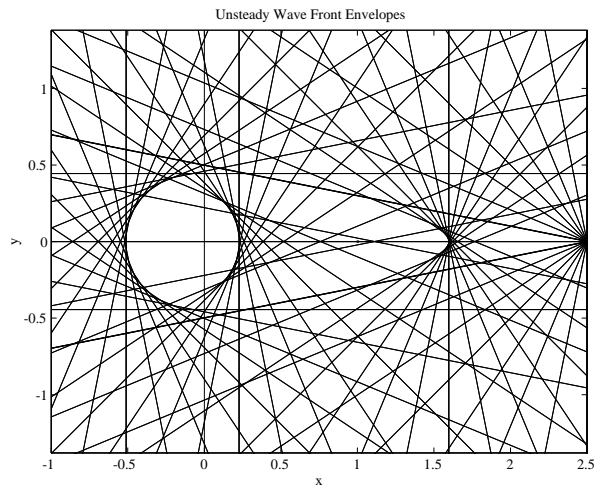
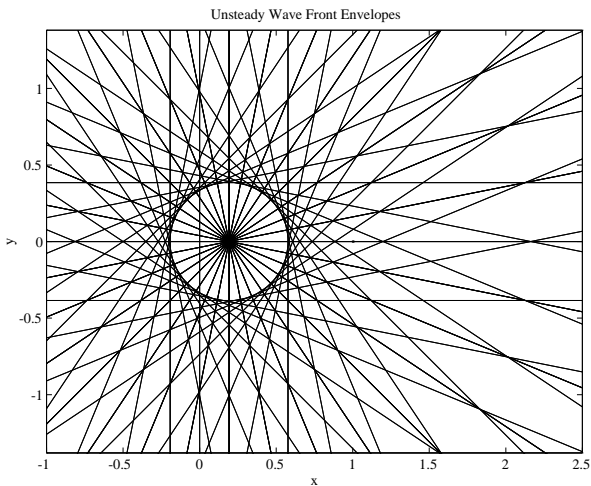
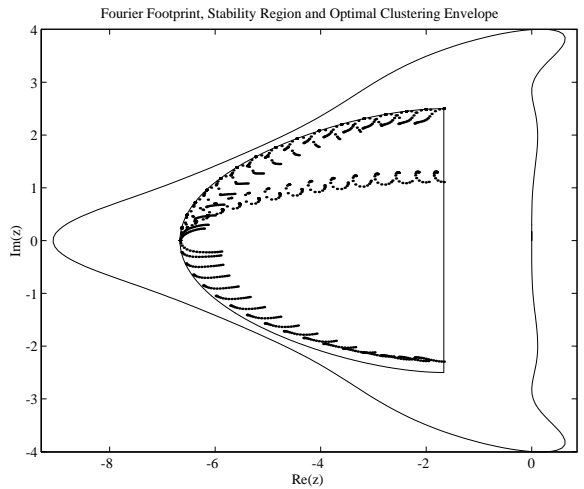
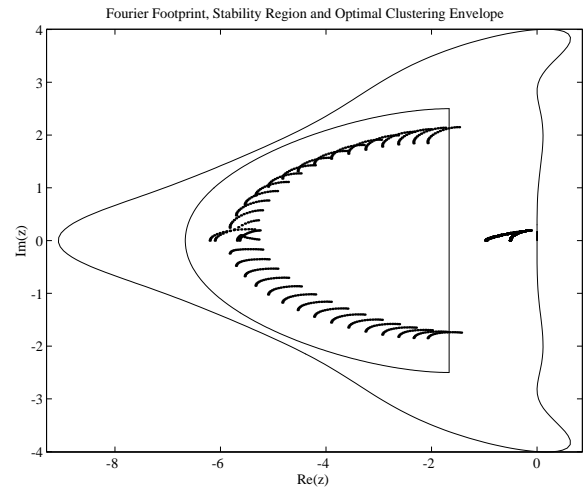
$$\widehat{W}^{n+1} = \psi(z) \widehat{W}^n.$$

Assuming constant  $Pr$  and  $\gamma$ , the four independent parameters that govern the discrete Navier–Stokes residual are the cell Reynolds number, Mach number, cell aspect ratio and flow angle:

$$Re_{\Delta x} = \frac{u\Delta x}{\nu}, \quad M = \frac{\sqrt{u^2 + v^2}}{c}, \quad \frac{\Delta y}{\Delta x}, \quad \frac{v}{u}.$$

The cell Reynolds number is based on  $u$  and  $\Delta x$  because the flow angle does not play a particularly interesting role in determining the form of the residual and is taken to be zero or asymptotically zero in all of the cases examined.

Analysis of eigenvalue clustering will initially focus on modes that are high frequency in both mesh directions ( $\frac{\pi}{2} \leq \theta_x, \theta_y \leq \pi$ ) since it is expected that a point-implicit method is not suitable for clustering eigenvalues corresponding to modes with a low frequency component. Fourier footprints corresponding to high frequency modes for aligned inviscid subsonic flow in a stretched mesh cell and 4th difference matrix dissipation are shown for both preconditioners in the top half of Fig. 1.



1a: Scalar Preconditioner.

1b: Block-Jacobi Preconditioner.

Figure 1: Fourier footprint of high frequency modes and wave front envelopes for 4th difference matrix dissipation.  $Re_{\Delta x} = \infty$ ,  $M = 0.5$ ,  $\frac{\Delta y}{\Delta x} = \frac{1}{5}$ ,  $\frac{v}{u} = 0$ ,  $\frac{\pi}{2} \leq \theta_x, \theta_y \leq \pi$ ,  $CFL = 2.5$ .

The inner solid line represents the optimal clustering envelope for high frequency modes based on a scalar advection-diffusion model problem [1]. The outer solid line represents the stability region for Martinelli's 5-stage Runge-Kutta time stepping scheme and is superimposed to assist in determining appropriate choices for the hyperbolic and parabolic CFL numbers [13]. For this case,  $Re_{\Delta x} = \infty$ , so that the preconditioners contain only the hyperbolic CFL number. For Navier–Stokes calculations, the fact that the maximum extent along the negative real axis is roughly twice the extent in either direction along the imaginary axis suggests the definition  $CFL_P = 2CFL_H$ , so that only the hyperbolic CFL number need be determined and the subscript may

be dropped.

In 2D there are four characteristic families representing convective entropy and vorticity modes and two acoustic pressure modes. The scalar preconditioner is unable to cluster the residual eigenvalues of the convective modes away from the origin but nearly succeeds in clustering the two acoustic footprints inside the optimal envelope. The block-Jacobi preconditioner provides optimal clustering for all four modes. The entropy footprint forms an arc on the optimal clustering envelope. The two acoustic footprints have nearly the same radius as the entropy mode, falling one each above and below the real axis, with the vorticity footprint forming a tongue between them.

Case 1	$Re_{\Delta x} = \infty$	$M \rightarrow 0$	$\frac{\Delta y}{\Delta x} \rightarrow 0$	$\frac{v}{u} = \frac{\Delta y}{\Delta x}$
Case 2	$Re_{\Delta x} = \infty$	$M \rightarrow 0$	$\frac{\Delta y}{\Delta x} \rightarrow 0$	$\frac{v}{u} = 0$
Case 3	$Re_{\Delta x} = \infty$	$M \rightarrow 0$	$\frac{\Delta y}{\Delta x} \rightarrow \infty$	$\frac{v}{u} = 0$
Case 4	$Re_{\Delta x} = \infty$	$M = 0.5$	$\frac{\Delta y}{\Delta x} \rightarrow \infty$	$\frac{v}{u} = 0$
Case 5	$Re_{\Delta x} \rightarrow \infty$	$M \rightarrow 0$	$\frac{\Delta y}{\Delta x} = Re_{\Delta x}^{-1/2}$	$\frac{v}{u} = 0$
Case 6	$Re_{\Delta x} \rightarrow \infty$	$M = 0.5$	$\frac{\Delta y}{\Delta x} = Re_{\Delta x}^{-1/2}$	$\frac{v}{u} = 0$

Table 1: Asymptotic limits for which analytic expressions for the Fourier footprint of 4th difference matrix dissipation are obtained.

### 3.2 Wave Front Envelopes

For the Euler equations, another interesting perspective on the role of preconditioning is provided by examining the effect on the shape of the wave front envelopes of the four characteristic families [20, 12]. The propagative speed for a wave traveling at an angle  $\theta = \tan^{-1} \frac{y}{x}$  is given for each of the characteristic families by an eigenvalue of the matrix

$$P(A \cos \theta + B \sin \theta).$$

The wave front for each eigenvalue is the line perpendicular to the direction of propagation. The wave front envelope for a family of waves is formed by the intersection of all the wave fronts in that family.

The preconditioned wave front envelopes for all four families are shown in the bottom half of Fig. 1. With the scalar preconditioner, the two convective envelopes collapse to a point and their evolution is severely limited by the circular acoustic envelopes. The matrix preconditioner moves the entropy envelope out to the maximum stability limit on the real axis and elongates the oval acoustic envelopes and the triangular vorticity envelope in the direction of cell stretching. This behavior is very appealing in a qualitative sense because it approximates the optimal condition for a stretched mesh, in which disturbances cross the same number of cells per unit time regardless of the direction of propagation.

### 3.3 Analytic Asymptotic Footprints

Having gained an intuitive feel for the effect of preconditioning, it is now worthwhile examining the behavior of the preconditioned system in more extreme conditions typical of a viscous boundary layer. Analytic expressions for the preconditioned Fourier footprints are obtained for the important set of asymptotic limits summarized in Table 1. Cases 1-4 assume  $Re_{\Delta x} = \infty$ , so that the viscous terms are neglected, though the effect of an “inviscid” boundary

layer is simulated for the first three cases by letting  $M \rightarrow 0$ . Cases 1 and 2 correspond to a stretched cell with either diagonal cross flow or aligned flow. In Case 3, the cell stretching is perpendicular to the flow, as at the leading edge of an airfoil. Case 4 examines a moderate subsonic flow perpendicular to a highly stretched cell as often occurs in the far field due to exponential stretching of the transverse mesh coordinates. Cases 5 and 6 consider the asymptotic footprint behavior for stretched cells in a viscous boundary layer. The scaling for the cell aspect ratio is found by balancing streamwise convection and normal diffusion, so that

$$\frac{u}{\Delta x} = \frac{\nu}{\Delta y^2},$$

which leads to the relation

$$\frac{\Delta y}{\Delta x} = Re_{\Delta x}^{-1/2}.$$

To simplify the analysis for Cases 5 and 6, the Prandtl number is assumed to be unity. All of the cases are analyzed for 4th difference matrix dissipation, since this is the type that is active over most of the fine mesh. For simplicity, the dissipative coefficient is taken to be  $\varepsilon^{(4)} = \frac{1}{8}$  with CFL = 1.0.

Analytic expressions for the asymptotic residual eigenvalue distributions are shown for all six cases in Table 2, where the notation  $s_x \equiv \sin \theta_x$ ,  $s_y \equiv \sin \theta_y$ ,  $C_x \equiv 1 - \cos \theta_x$ ,  $C_y \equiv 1 - \cos \theta_y$  is adopted for brevity. The Fourier footprints corresponding to the high frequency modes are plotted in Figs 2 and 3 using a separate symbol for each family, as defined in Table 3. This table describes the asymptotic dependences of the different families on the two Fourier angles, corresponding to the directions of effective smoothing.

Using the scalar preconditioner, the footprints of both convective modes fall on the origin for every case except the subsonic cross flow of Case 4.

Case	$-\text{eig}(P_S Z)$	$-\text{eig}(P_J Z)$
1	0	$\frac{1}{2}[\frac{2}{3}(C_x^2 + C_y^2) + i(s_x + s_y)]$
	0	$\frac{2}{3}C_x^2$
	$\frac{2}{3}C_y^2 + is_y$	$\frac{2}{3}C_y^2 + is_y$
	$\frac{2}{3}C_y^2 - is_y$	$\frac{2}{3}C_y^2 - is_y$
2	0	$\frac{2}{3}C_x^2 + is_x$
	0	$\frac{2}{3}C_x^2$
	$\frac{2}{3}C_y^2 + is_y$	$\frac{2}{3}C_y^2 + is_y$
	$\frac{2}{3}C_y^2 - is_y$	$\frac{2}{3}C_y^2 - is_y$
3	0	$\frac{2}{3}C_x^2 + is_x$
	0	$\frac{1}{2}[\frac{2}{3}(C_x^2 + C_y^2) + is_x]$
	$\frac{2}{3}C_x^2 + is_x$	$\frac{2}{3}C_x^2 + is_x$
	$\frac{2}{3}C_x^2 - is_x$	$\frac{2}{3}C_x^2 - is_x$
4	$\frac{1}{3}(\frac{2}{3}C_x^2 + is_x)$	$\frac{2}{3}C_x^2 + is_x$
	$\frac{1}{3}(\frac{2}{3}C_x^2 + is_x)$	$\frac{2}{3}C_x^2 + is_x$
	$\frac{2}{3}C_x^2 + is_x$	$\frac{2}{3}C_x^2 + is_x$
	$\frac{1}{3}(\frac{2}{3}C_x^2 - is_x)$	$\frac{2}{3}C_x^2 - is_x$
5	0	$\frac{1}{3}(\frac{2}{3}C_x^2 + 2C_y + is_x)$
	0	$\frac{2}{3}C_x^2$
	$\frac{2}{3}C_y^2 + is_y$	$\frac{2}{3}C_y^2 + is_y$
	$\frac{2}{3}C_y^2 - is_y$	$\frac{2}{3}C_y^2 - is_y$
6	0	$\frac{1}{3}(\frac{2}{3}C_x^2 + 2C_y + is_x)$
	0	$\frac{1}{4}(\frac{4}{3}C_x^2 + 2C_y + is_x)$
	$\frac{2}{3}C_y^2 + is_y$	$\frac{2}{3}C_y^2 + is_y$
	$\frac{2}{3}C_y^2 - is_y$	$\frac{2}{3}C_y^2 - is_y$

Table 2: Analytic expressions for the Fourier footprint of 4th difference matrix dissipation with Scalar and Block-Jacobi preconditioning.

Therefore, the system will not converge using full coarsening multigrid and a standard scalar preconditioner. On the other hand, the block-Jacobi preconditioner provides optimal clustering of residual eigenvalues corresponding to high frequency modes in all cases. Recall, however, that an efficient full coarsening multigrid algorithm is also dependent on rapid damping of modes that are high frequency in one mesh direction and low frequency in the other.

The performance of the preconditioners on these modes is evident from Table 3. Asymptotic dependence on a Fourier angle amounts to effective damping of modes in that direction, since the corresponding eigenvalues will not be clustered at the origin. For the viscous conditions of Cases 5 and 6, neither preconditioner is able to cope with a sawtooth pressure mode in the streamwise direction, but the matrix preconditioner is able to damp sawtooth entropy modes in either direction, even for perfectly aligned flow. The same is true of convective vorticity modes as long as the Mach number does not vanish. Notice that this is not the situation for the inviscid aligned flow of Case 2, where a normal sawtooth entropy mode will not be damped in a highly stretched cell.

Inside a viscous boundary layer, the point-implicit block-Jacobi preconditioner provides adequate clustering for all convective modes that are high/low or low/high as long as the Mach number is not asymptotically zero. The only modes which are not treated effectively are acoustic pressure modes with a high frequency streamwise component and a low frequency normal component. Rather than adopting the complete semi-coarsening algorithm of Mulder, it seems likely that some less expensive enhancement of the full coarsening strategy can be devised which will overcome this shortcoming.

One possibility is to implement only a subset of the complete semi-coarsening stencil, such as including only those meshes which provide coarsening across the boundary layer. An even less expensive alternative is a normal or J-coarsened strategy in which no coarsening is performed in the streamwise direction. With this approach, high- $x$ /low- $y$  pressure modes become high- $x$ /high- $y$  modes on the coarse mesh, which can then be effectively damped. At first glance, the apparent weakness of this approach is the treatment of low- $x$ /low- $y$  modes, which would have become high- $x$ /high- $y$  modes on the coarse mesh with a full coarsening algorithm. However, closer inspection reveals that low- $x$ /low- $y$  modes become low- $x$ /high- $y$  modes on the coarse mesh, which can then be effectively damped in any characteristic field. Therefore, inside the boundary layer, block-Jacobi preconditioning provides effective damping of all eigenvalues that cannot be resolved on the coarse mesh using a J-coarsened multigrid algorithm. This is possible because of the balance of streamwise convection and normal diffusion inside the boundary layer. For Euler computations, some sawtooth modes will not be clustered effectively, but the impact on convergence when using a typical inviscid mesh is probably not sufficient to warrant switching from a full coarsening multigrid

Mode	Entropy ( $\cdot$ )		Vorticity ( $*$ )		Acoustic ( $\circ$ )		Acoustic ( $+$ )	
Speed	$q$		$q$		$q + c$		$q - c$	
Precon	$P_S$	$P_J$	$P_S$	$P_J$	$P_S$	$P_J$	$P_S$	$P_J$
Case 1	0	$\theta_x, \theta_y$	0	$\theta_x$	$\theta_y$	$\theta_y$	$\theta_y$	$\theta_y$
Case 2	0	$\theta_x$	0	$\theta_x$	$\theta_y$	$\theta_y$	$\theta_y$	$\theta_y$
Case 3	0	$\theta_x$	0	$\theta_x, \theta_y$	$\theta_x$	$\theta_x$	$\theta_x$	$\theta_x$
Case 4	$\theta_x$	$\theta_x$	$\theta_x$	$\theta_x$	$\theta_x$	$\theta_x$	$\theta_x$	$\theta_x$
Case 5	0	$\theta_x, \theta_y$	0	$\theta_x$	$\theta_y$	$\theta_y$	$\theta_y$	$\theta_y$
Case 6	0	$\theta_x, \theta_y$	0	$\theta_x, \theta_y$	$\theta_y$	$\theta_y$	$\theta_y$	$\theta_y$

Table 3: Definition of mode symbols and representative propagative speeds for Figs 2 and 3, and the asymptotic dependence of each mode on  $\theta_x$  and  $\theta_y$ , corresponding to the directions of effective smoothing.

strategy.

The context in which point-implicit block-Jacobi preconditioning can probably be used to greatest advantage is in unstructured codes that employ either agglomeration or edge collapsing multigrid strategies to provide local semi-coarsening. In this scenario, the preconditioner provides adequate clustering of all residual eigenvalues and should facilitate rapid convergence for explicit solvers even on highly stretched meshes.

## 4 Results

Results for a number of standard test cases are generated using a conservative cell-centered semi-discrete finite volume scheme. Characteristic-based matrix dissipation based on Roe’s linearization [17] provides a basis for the construction of high resolution switched, symmetric limited and upstream limited schemes following the work of Jameson [11, 7, 8, 10]. Updates are performed using a 5-stage Runge-Kutta time stepping scheme to drive a full coarsening multigrid algorithm [11, 5, 13].

For Euler and laminar Navier–Stokes calculations, the solution is computed on a sequence of fine meshes using a W-cycle on each mesh. A single time step is performed at each level when moving down the multigrid cycle. The stability limit on both fine and coarse meshes is  $CFL = 2.5$ .

For turbulent calculations on highly stretched meshes, a J-coarsening strategy in which meshes are coarsened only across the boundary layer is also tested. Since the cost of a W-cycle becomes very large when using a semi-coarsening approach, all turbulent calculations are performed using a V-cycle with time steps computed moving both up and down the cycle. The one-equation Spalart-Allmaras tur-

bulence model is solved using a first order spatial discretization and 5-stage Runge-Kutta time integration with implicit treatment of the source terms to drive the same multigrid algorithm as that used for the flow equations [18]. This solution procedure is very convenient because the turbulent viscosity can be treated in nearly all subroutines as an extra variable in the state vector.

The plotted residuals represent the rms change in density during one application of the time stepping scheme on the finest mesh in the multigrid cycle. Descriptions of the geometry, flow parameters, mesh properties and observed speed-ups for each test case are provided in Table 4. The speed-ups are calculated at a residual level of  $10^{-4}$  relative to the initial residual. The additional cost of block-Jacobi preconditioning is 20-25% if the preconditioner is updated once per time step.

### 4.1 Euler

In Fig. 4, solutions to a standard NACA0012 test case with a weak shock on the lower surface are shown after 12 and 100 W-cycles using a matrix switched scheme and block-Jacobi preconditioning. After 12 cycles, the lift changes by only four counts and the drag is fully converged. This rate of convergence is achieved without using other acceleration techniques such as implicit residual smoothing and enthalpy damping [6].

Fig. 5 displays the Mach contours for flow past a cylinder at  $M_\infty = 0.38$  using matrix symmetric limited dissipation. The cell aspect ratio at the wall is  $\frac{1}{10}$  and the first cells are 0.003 chords in height. The accuracy of the scheme is demonstrated by the symmetry of the solution upstream and downstream of the cylinder. The maximum entropy deviation in

Geometry	$M_\infty$	$\alpha$	$Re_L$	Mesh	$\frac{\Delta\eta}{\Delta\xi} _{\max}$	$\frac{\Delta\eta}{\Delta\xi} _{\min}$	$\frac{\Delta\eta}{L} _{\text{wall}}$	$P_J$
NACA0012	0.8	$1.25^\circ$	$\infty$	$160 \times 32$	$2 \times 10^{+1}$	$5 \times 10^{-1}$	$7 \times 10^{-4}$	3.7
Cylinder	0.38	$0.0^\circ$	$\infty$	$128 \times 48$	$3 \times 10^{+0}$	$1 \times 10^{-1}$	$3 \times 10^{-3}$	6.2
NACA0012	0.8	$10.0^\circ$	$5 \times 10^2$	$320 \times 64$	$2 \times 10^{+1}$	$5 \times 10^{-1}$	$2 \times 10^{-4}$	3.9
Flat Plate	0.15	$0.0^\circ$	$1 \times 10^5$	$128 \times 32$	$4 \times 10^{+2}$	$3 \times 10^{-3}$	$3 \times 10^{-5}$	7.2
RAE2822	0.725	$2.4^\circ$	$6.5 \times 10^6$	$256 \times 64$	$3 \times 10^{+1}$	$7 \times 10^{-4}$	$4 \times 10^{-6}$	2.9
RAE2822	0.73	$2.79^\circ$	$6.5 \times 10^6$	$256 \times 64$	$3 \times 10^{+1}$	$7 \times 10^{-4}$	$4 \times 10^{-6}$	2.4

Table 4: Test case definitions, mesh dimensions, maximum and minimum cell aspect ratios, minimum ratio of cell height to chord length at the wall and speed-ups for  $P_J$  compared to  $P_S$ .

the cells next to the wall is  $5 \times 10^{-4}$ .

Since the symmetric limited and switched formulations are fundamentally similar [10], it was expected that the block-Jacobi preconditioner based on the switched scheme would also be appropriate for symmetric limited dissipation. However, the speed-ups observed using an upstream limited scheme that does not resemble the 2nd/4th difference switching mechanism were also comparable, which suggests that it may be sufficient to base the form of the block-Jacobi preconditioner on the first order dissipative scheme. From this point of view, the principal advantage of reducing  $\varepsilon^{(4)}$  to  $\frac{1}{6}$  (from the more likely value of  $\frac{1}{4}$ ), is the corresponding increase in the allowable time step from  $\text{CFL} = 1.8$  to  $\text{CFL} = 2.5$ , which more than compensates for the reduced damping of the scheme. The footprint of the symmetric and upstream limited schemes is apparently larger than that of the switched scheme using either scalar or matrix preconditioning, since the CFL number could not be raised above 1.5 on the fine meshes.

## 4.2 Laminar Navier–Stokes

Fig. 6 displays the results for a transonic laminar NACA0012 test case. The resolution of the mesh appears to be adequate for  $Re_L = 500$  based on a comparison of the Mach number contours with results in reference [13]. This viewpoint is further supported by the budget plot at the lower mid-chord, which reveals that there are roughly 20 points in the boundary layer. Once again, the block-Jacobi preconditioner realizes a significant speed-up over the standard scalar time step.

Results for nearly incompressible flow over a flat plate at  $Re_L = 1 \times 10^5$  are displayed in Fig. 7 for a  $128 \times 32$  H-mesh. Three quarters of the streamwise points are located on the plate and half the normal points are equally spaced in the boundary

layer coordinate inside the boundary layer [19]. Exponential stretching is used in all directions outside the boundary layer, and some extremely high aspect ratio cells of  $O(10^{\pm 5})$  are alleviated by skewing the stretching at the far field. It was necessary to reduce the CFL number to 2.0 on the fine mesh as a result of the extreme non-orthogonality in some cells. The maximum and minimum cell aspect ratios are 400 and  $\frac{1}{330}$  and the minimum height of the first cell is 0.00003 chords. The inlet is one chord ahead of the plate, the outlet is at the trailing edge and the upper boundary is located two chords from the plate. A comparison of the velocity components at the mid-chord with the exact Blasius solution reveals a slight inaccuracy in the normal velocity component. Convergence plots demonstrating substantial acceleration are shown for both the density residual and the drag coefficient. An examination of the residuals at the end of the computations revealed that the convergence was dominated by the near field when using a scalar preconditioner and the far field mesh singularity above the leading edge when using the matrix preconditioner.

## 4.3 Turbulent Navier–Stokes

Results for RAE2822 AGARD Case 6 are shown in Fig. 8. The computations are performed on a  $256 \times 64$  C-mesh with maximum and minimum cell aspect ratios of  $3 \times 10^{+1}$  and  $7 \times 10^{-4}$  and a minimum first cell height of  $4 \times 10^{-6}$  chords [3]. Convergence plots contain the residuals for density and the turbulent viscosity. Using full coarsening multigrid, the block-Jacobi preconditioner provides only a slight improvement over the scalar preconditioner, which suggests that streamwise acoustic pressure modes are dominating the convergence process. Using J-coarsened multigrid improves the performance of both preconditioners and allows the superior clustering properties of the block-Jacobi preconditioner to take ef-

fect, so that all modes are effectively damped inside the boundary layer. Furthermore, J-coarsened multigrid allows the turbulent viscosity to converge at the same asymptotic rate as the density. A comparison of density residuals for all permutations of preconditioning and multigrid strategies is shown to demonstrate the relative costs of these methods. The combination of block-Jacobi preconditioning and J-coarsened multigrid, which has the highest cost per cycle, is still the most efficient method by a large margin. The pressure distribution compares well with the experimental results [4]. The largest discrepancies occur at the leading edge and along the lower surface. The transition point is set using the trip term built into the Spalart–Allmaras model.

Results for RAE2822 AGARD Case9 are shown in Fig. 9. Once again, substantial savings are realized using block-Jacobi preconditioning and J-coarsened multigrid. The shock location is predicted quite well and the deviation at the leading edge is reduced for this case.

It is illuminating to compare the convergence rates achieved for these turbulent calculations on highly stretched meshes with the results for inviscid calculations on more isotropic meshes. Using block-Jacobi preconditioning and J-coarsened multigrid on a mesh with a minimum cell aspect ratio of  $7 \times 10^{-4}$ , convergence to  $O(10^{-4})$  is achieved in about 220 V-cycles. By comparison, an Euler computation on the mesh of Fig. 4, which has a minimum cell aspect ratio of  $\frac{1}{2}$ , takes 165 W-cycles to reach the same level of convergence with a standard scalar preconditioner and 40 W-cycles using block-Jacobi preconditioning. Therefore, using the strategies developed in this paper, convergence of turbulent Navier–Stokes calculations on highly stretched meshes approaches the rate of convergence achieved for Euler computations using a standard scalar time step. It is expected that the results for turbulent calculations can be improved still further by adopting a multigrid strategy which combines aspects of both the full and J-coarsened approaches.

## 5 Conclusions

Analysis of the asymptotic behavior of the Fourier footprints for scalar and block-Jacobi preconditioners reveals critical information about the successes and failures of these approaches. The scalar preconditioner is completely ineffective at clustering high frequency convective modes away from the origin for all cases involving vanishing Mach number.

The block-Jacobi preconditioner succeeds in clus-

tering all high frequency modes inside the optimal envelope based on a scalar advection-diffusion model problem. Furthermore, in the stretched cells of a viscous boundary layer, the block-Jacobi preconditioner also provides adequate clustering of convective modes that are high frequency in one mesh direction and low frequency in the other. However, acoustic pressure modes that are high frequency in the streamwise direction and low frequency across the boundary layer are not clustered effectively. Therefore, a J-coarsening strategy is adopted, which alleviates this problem and allows adequate clustering of all modes inside the boundary layer.

Implementations based on this analysis have yielded very encouraging results on a wide variety of Euler, laminar and turbulent Navier–Stokes test cases. Considerable speed-ups have been achieved using both full and J-coarsened multigrid in conjunction with high resolution characteristic-based dissipation on fine meshes.

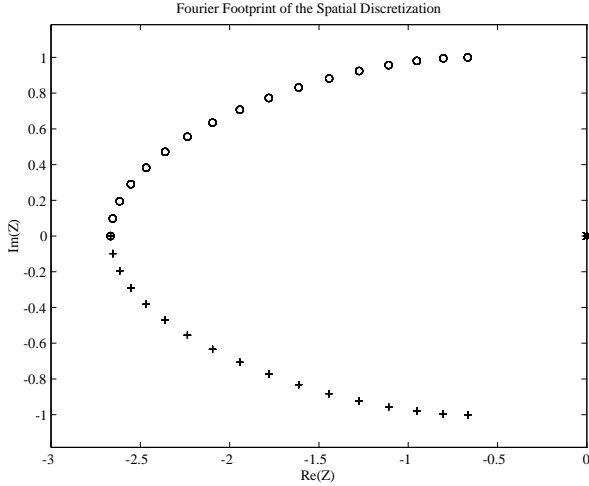
## Acknowledgements

We wish to thank Dr. Luigi Martinelli for assistance with many aspects of the code development, Dr. Antony Jameson for providing the mesh generator, Dr. Feng Liu for considerable advice on implementing turbulent transport equations, Dr. Dimitri Mavriplis for helpful comments on the Spalart–Allmaras turbulence model and Dr. Russell Cummings for providing computer facilities during the final stages of this work. The first author gratefully acknowledges the funding of the Rhodes Trust.

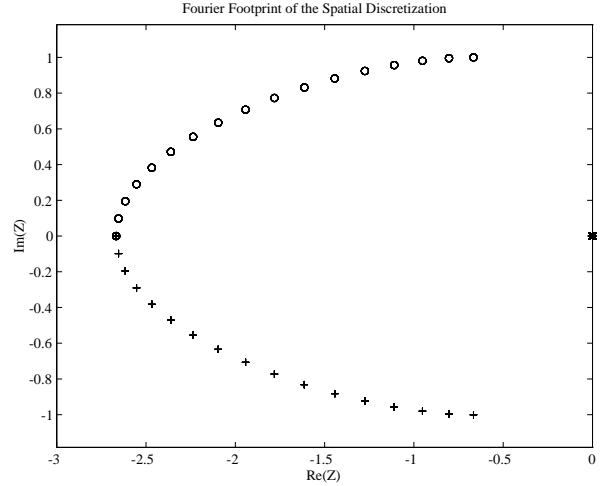
## References

- [1] S. Allmaras. Analysis of a local matrix preconditioner for the 2-D Navier–Stokes equations. AIAA Paper 93-3330-CP, 11th Computational Fluid Dynamics Conference, Orlando, FL, 1993.
- [2] S. Allmaras. Analysis of semi-implicit preconditioners for multigrid solution of the 2-D compressible Navier–Stokes equations. AIAA Paper 95-1651-CP, 12th Computational Fluid Dynamics Conference, San Diego, CA, 1995.
- [3] J.J. Benton. Validation of 2D Navier–Stokes codes for aerofoils. BRITE/EURAM 1066, Validation of CFD EUROVAL, Progress at British Aerospace to 15-January, 1991.
- [4] P.H. Cook, M.A. McDonald, and M.C.P. Firmin. AEROFOIL RAE2822 pressure dis-

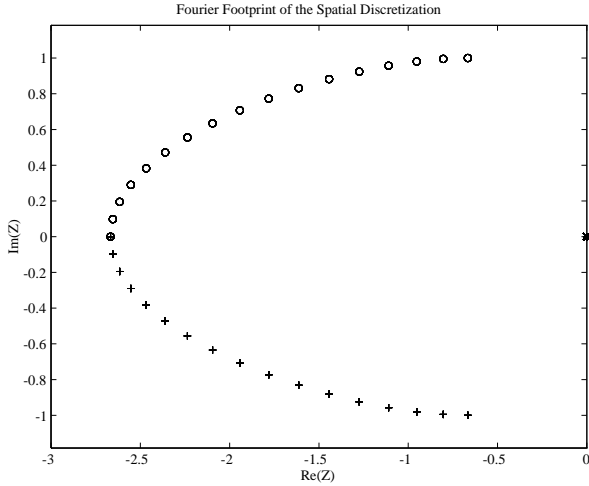
- tributions, boundary layer and wake measurements. AGARD Advisory Report No. 138, 1979.
- [5] A. Jameson. Solution of the Euler equations for two dimensional transonic flow by a multigrid method. MAE Report #1613, Princeton University, 1983.
- [6] A. Jameson. Transonic flow calculations. MAE Report #1651, Princeton University, 1983.
- [7] A. Jameson. A non-oscillatory shock capturing scheme using flux limited dissipation. MAE Report #1653, Princeton University, 1984.
- [8] A. Jameson. Computational algorithms for aerodynamic analysis and design. MAE Report #1966, Princeton University, 1992.
- [9] A. Jameson. Numerical wind tunnel – vision or reality. AIAA Paper 93-3021, AIAA 11th Computational Fluid Dynamics Conference, Orlando, Florida, 1993.
- [10] A. Jameson. Analysis and design of numerical schemes for gas dynamics 1: Artificial diffusion, upwind biasing limiters and their effect on accuracy and multigrid convergence. Submitted for publication in the International Journal of Computational Fluid Dynamics, 1994.
- [11] A. Jameson, W. Schmidt, and E. Turkel. Numerical solution of the Euler equations by finite volume methods using Runge-Kutta time stepping schemes. AIAA Paper 81-1259, 1981.
- [12] W.-T. Lee. *Local Preconditioning of the Euler Equations*. PhD thesis, University of Michigan, 1992.
- [13] L. Martinelli. *Calculations of Viscous Flows with a Multigrid Method*. PhD thesis, Princeton University, 1987.
- [14] W.A. Mulder. A new multigrid approach to convection problems. *J. Comp. Phys.*, 83:303–323, 1989.
- [15] W.A. Mulder. A high-resolution Euler solver based on multigrid, semi-coarsening and defect correction. *J. Comp. Phys.*, 100:91–104, 1992.
- [16] N.A. Pierce and M.B. Giles. Preconditioning on stretched meshes. Oxford University Computing Laboratory Technical Report 95/10, Presented at the 12th AIAA CFD Conference, San Diego, CA, 1995.
- [17] P.L. Roe. Approximate Riemann solvers, parameter vectors, and difference schemes. *J. Comp. Phys.*, 43:357–372, 1981.
- [18] P.R. Spalart and S.R. Allmaras. A one-equation turbulence model for aerodynamic flows. *La Recherche Aeronautique*, 1:5–21, 1994.
- [19] S. Tatsumi, L. Martinelli, and A. Jameson. Design, implementation, and validation of flux limited schemes for the solution of the compressible Navier-Stokes equations. AIAA Paper 94-0647, 32nd Aerospace Sciences Meeting and Exhibit, Reno, Nevada, 1994.
- [20] B. van Leer, W.T. Lee, and P.L. Roe. Characteristic time-stepping or local preconditioning of the Euler equations. AIAA Paper 91-1552-CP, 1991.



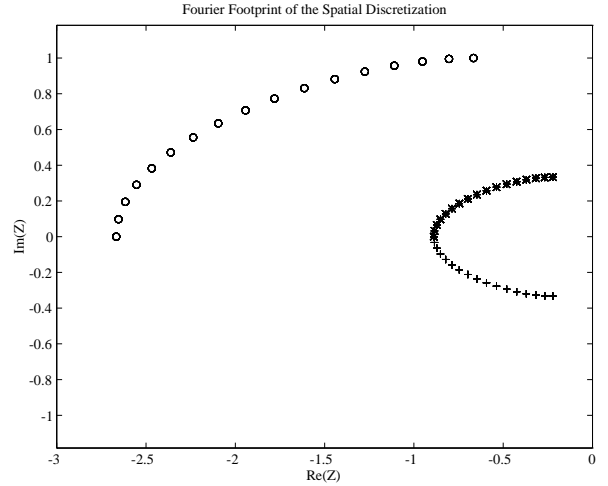
2a: Case 1.



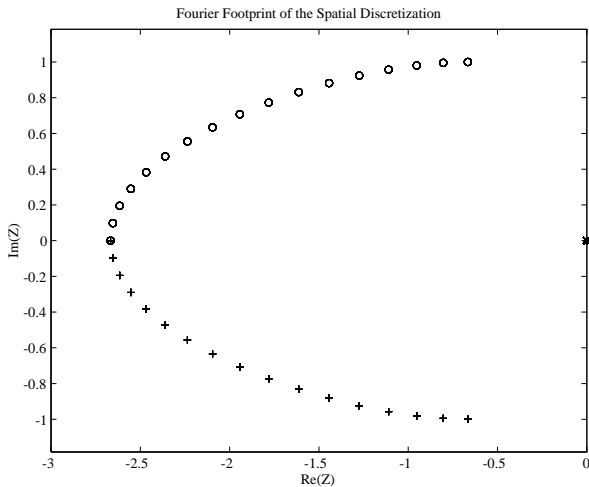
2b: Case 2.



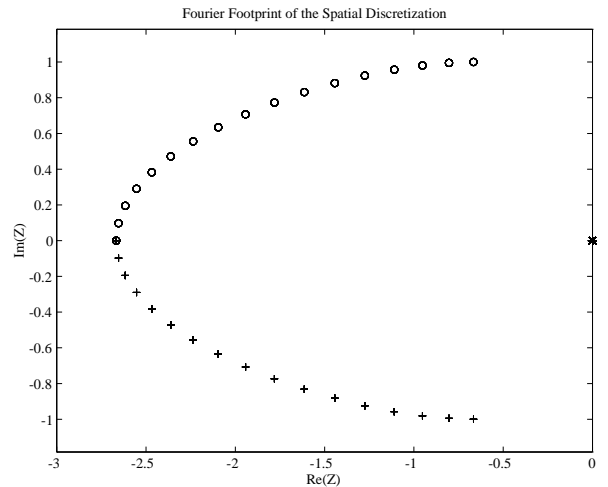
2c: Case 3.



2d: Case 4.



2e: Case 5.

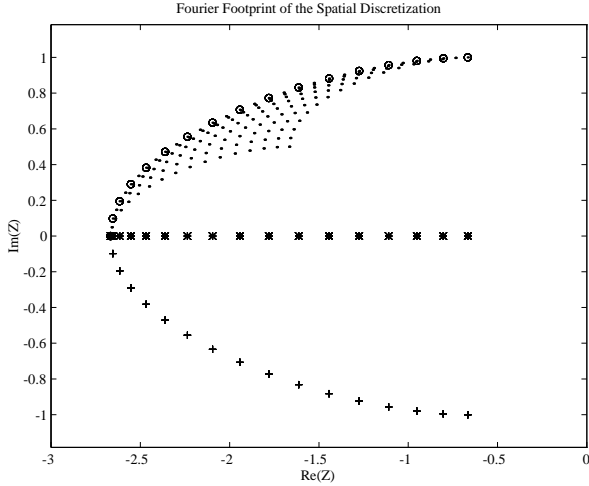


2f: Case 6.

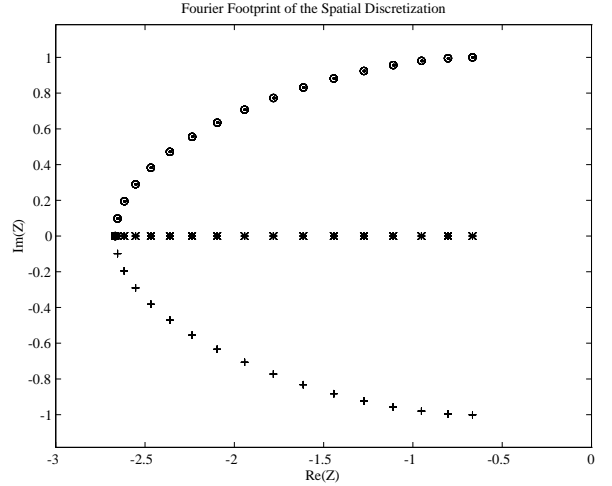
Figure 2: Scalar Preconditioner.

Fourier footprint of high frequency modes in various asymptotic limits.  
 4th difference matrix dissipation.  $\varepsilon^{(4)} = \frac{1}{6}$ ,  $\pi/2 \leq \theta_x, \theta_y \leq \pi$ , CFL = 1.0.

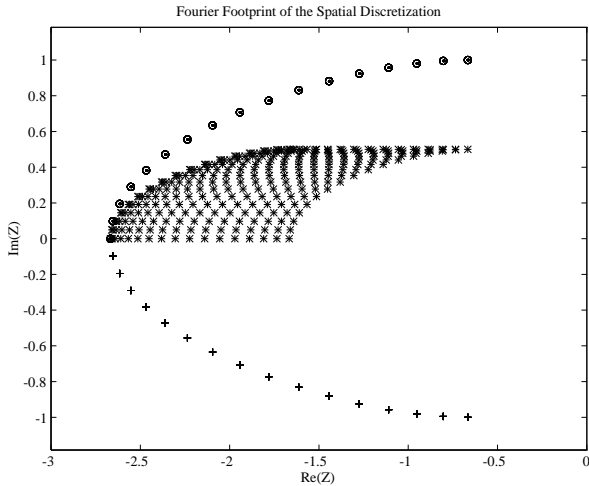
See Tables 1,2,3 for Case, Analytic and Wave descriptions.



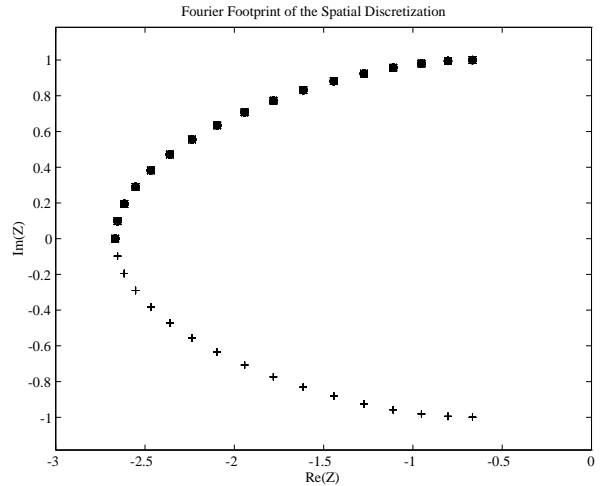
3a: Case 1.



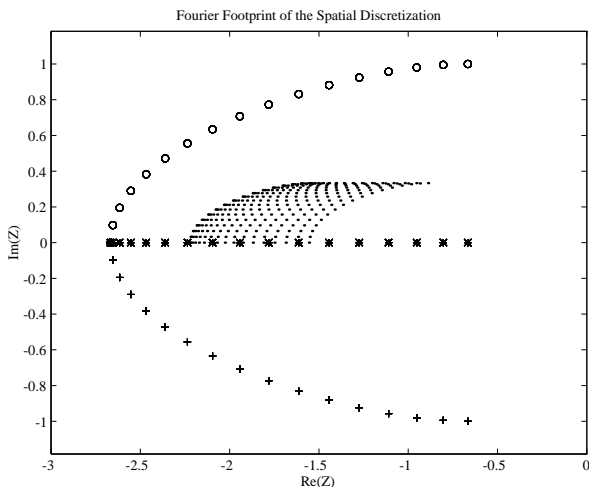
3b: Case 2.



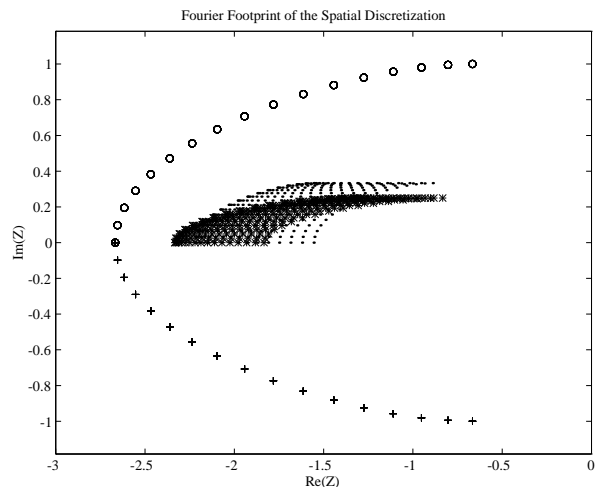
3c: Case 3.



3d: Case 4.



3e: Case 5.

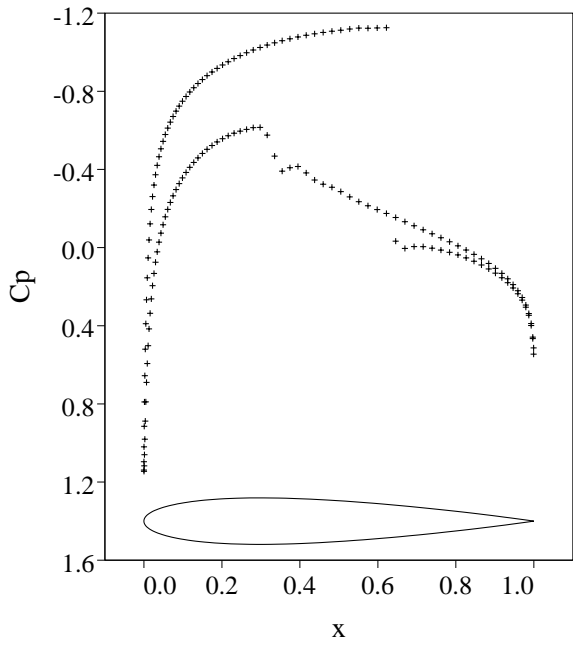


3f: Case 6.

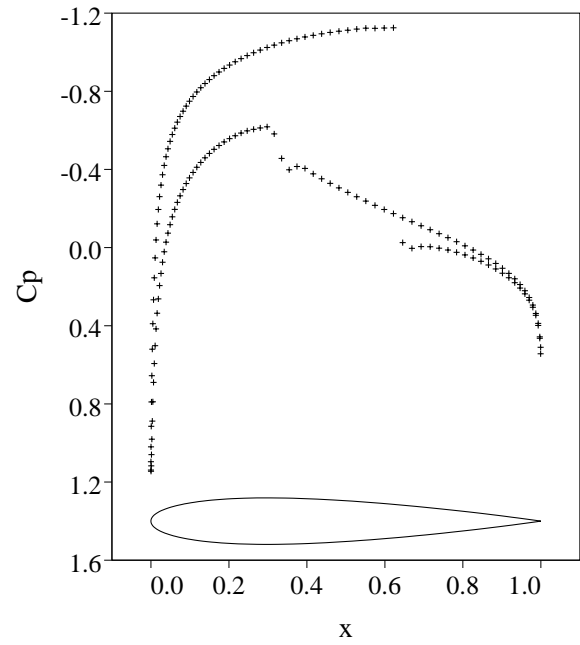
Figure 3: Block-Jacobi Preconditioner.

Fourier footprint of high frequency modes in various asymptotic limits.  
 4th difference matrix dissipation.  $\varepsilon^{(4)} = \frac{1}{6}$ ,  $\pi/2 \leq \theta_x, \theta_y \leq \pi$ , CFL = 1.0.

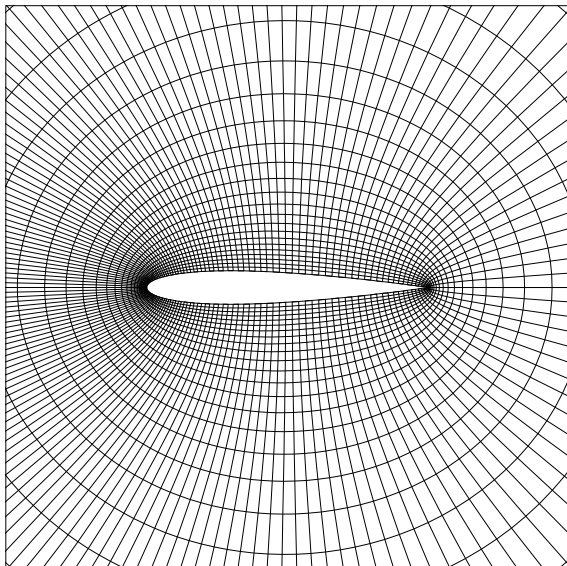
See Tables 1,2,3 for Case, Analytic and Wave descriptions.



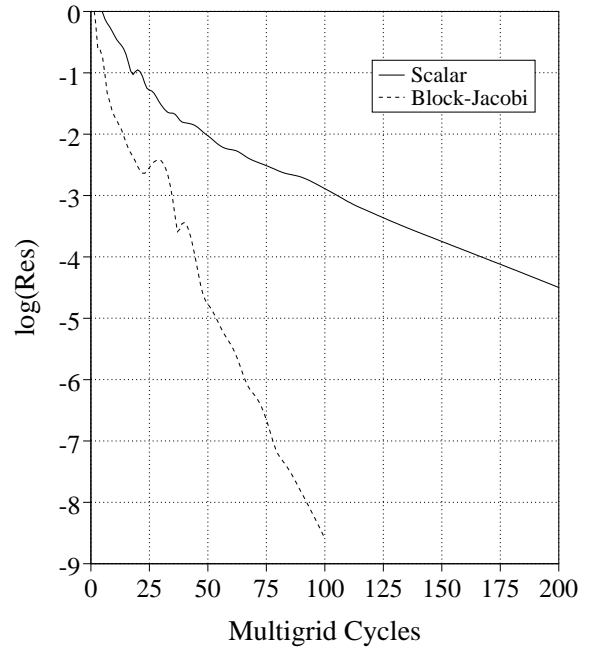
4a:  $C_p$  after 12 Multigrid Cycles.  
 $C_l = .3531, C_d = .0227$



4b:  $C_p$  after 100 Multigrid Cycles.  
 $C_l = .3527, C_d = .0227$

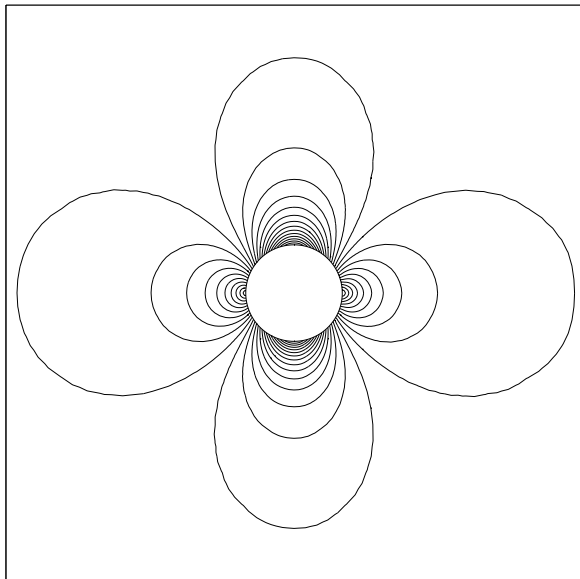


4c: Mesh.

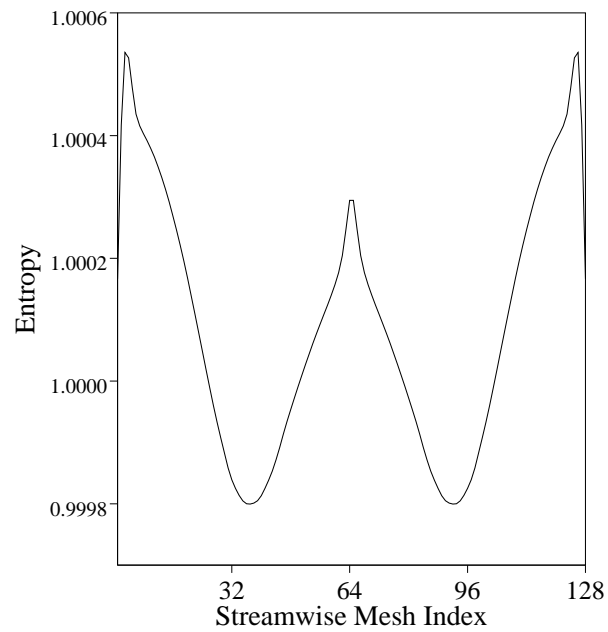


4d: Convergence.

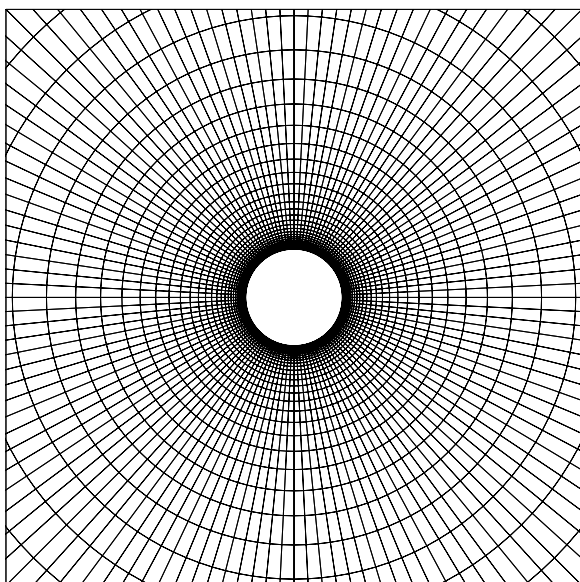
Figure 4: NACA0012 Airfoil.  $M_\infty = 0.8, \alpha = 1.25^\circ, 160 \times 32$  O-mesh.  
 Matrix Switched Scheme.



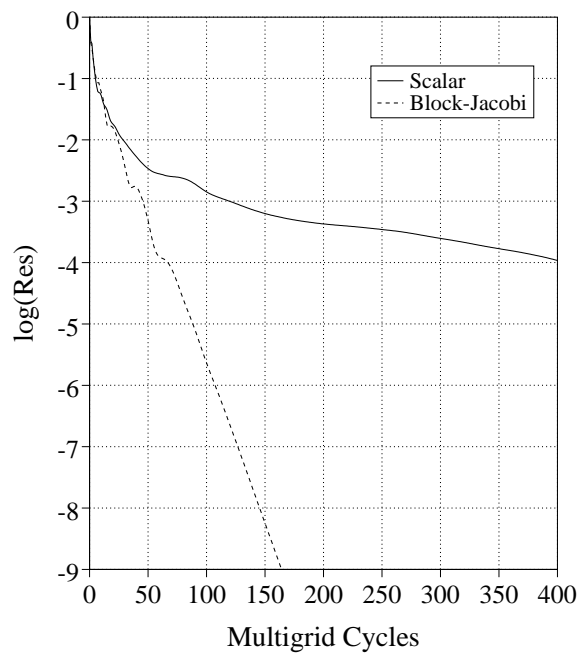
5a: Mach Number Contours.



5b: Entropy Next to the Wall.  
 $s = \frac{p}{\rho^\gamma}$

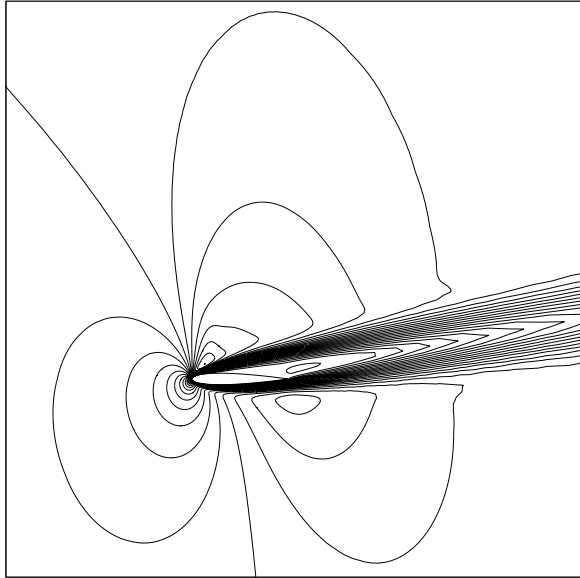


5c: Mesh.

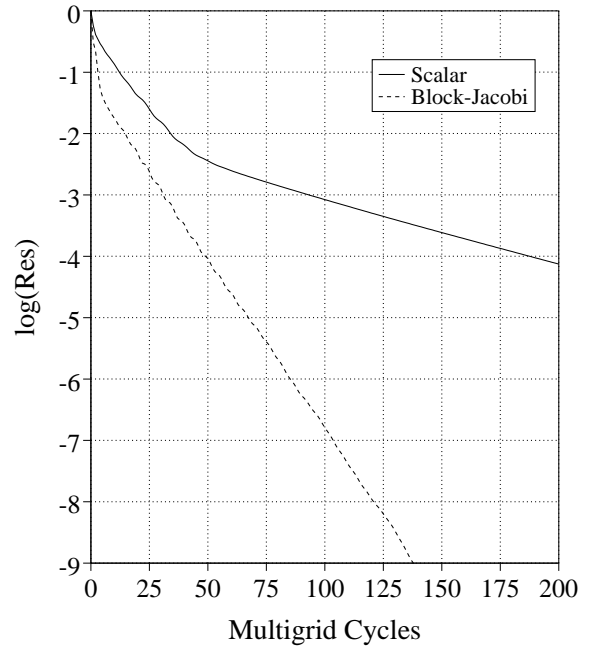


5d: Convergence.

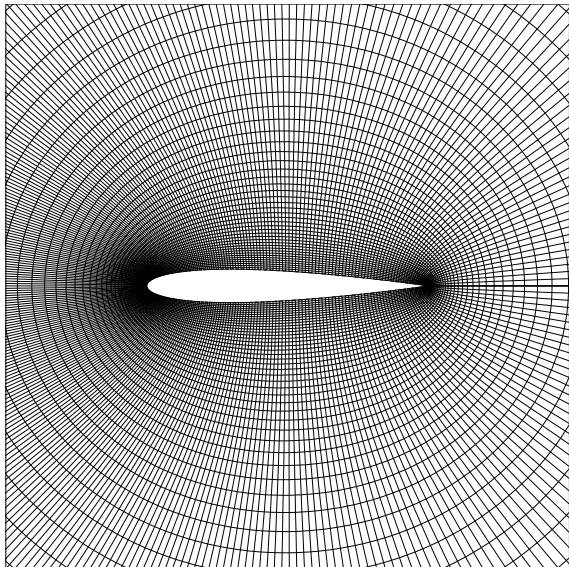
Figure 5: Cylinder.  $M_\infty = 0.38$ ,  $\alpha = 0.0^\circ$ ,  $128 \times 48$  O-mesh.  
 Matrix Symmetric Limited Scheme.



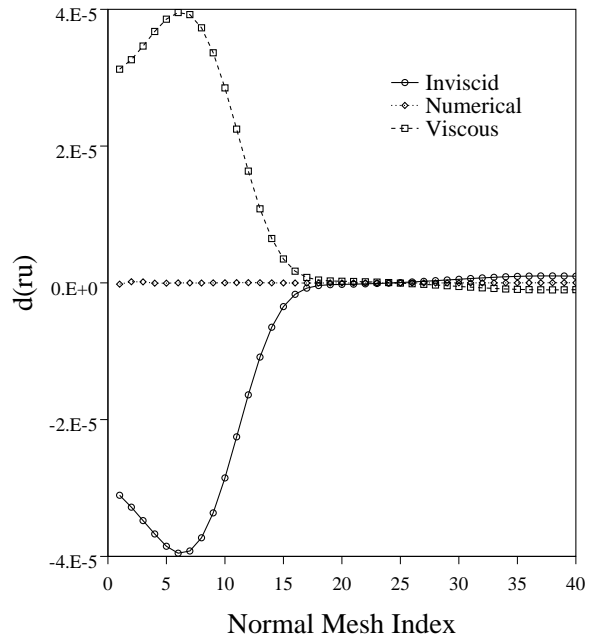
6a: Mach Number Contours.



6b: Pressure Contours.

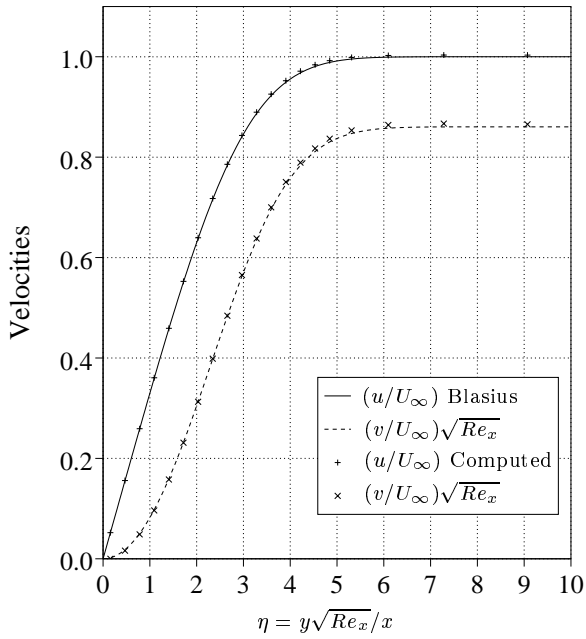


6c: Convergence.

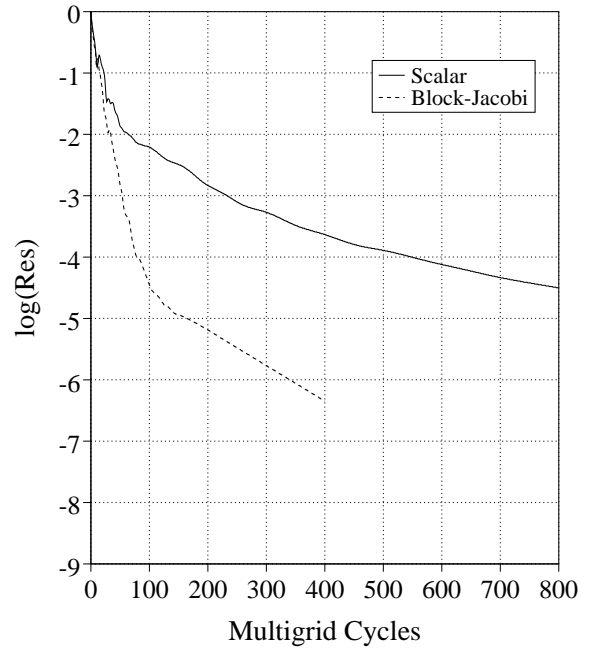


6d: Budget of X-Momentum Cell Updates.

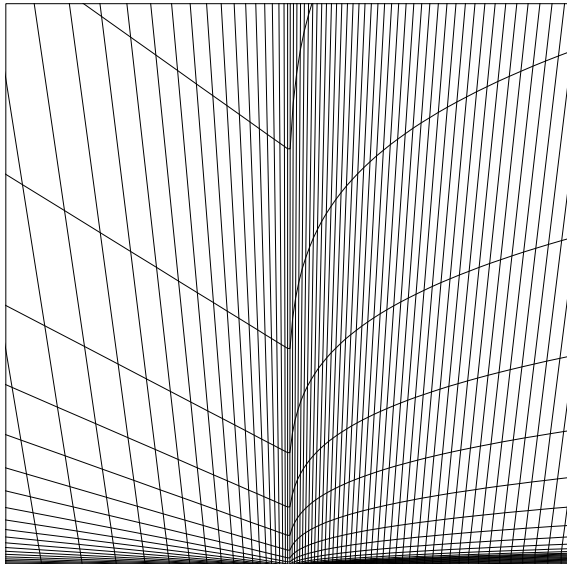
Figure 6: NACA0012 Airfoil.  $M_\infty = 0.8$ ,  $\alpha = 10.0^\circ$ ,  $Re_L = 5 \times 10^2$ ,  $320 \times 64$  O-mesh. Matrix Switched Scheme.



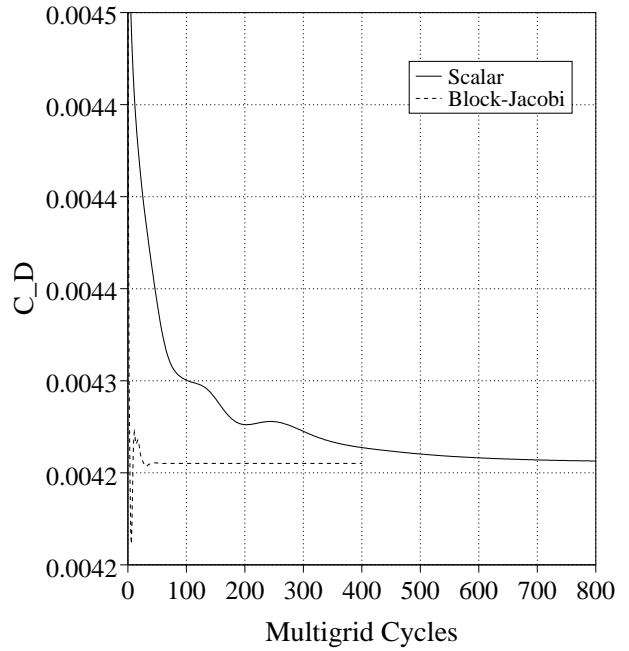
7a: Comparison to Blasius Velocity Profiles.



7b: Convergence.

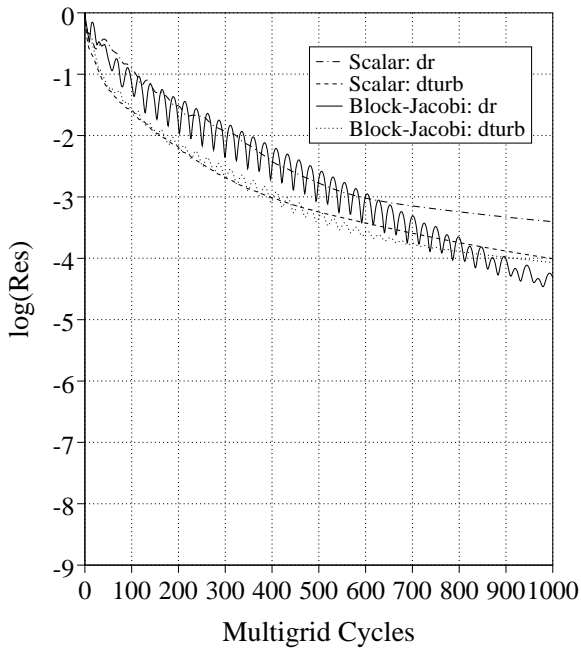


7c: Mesh at the Leading Edge. Magnification is 20% chord.

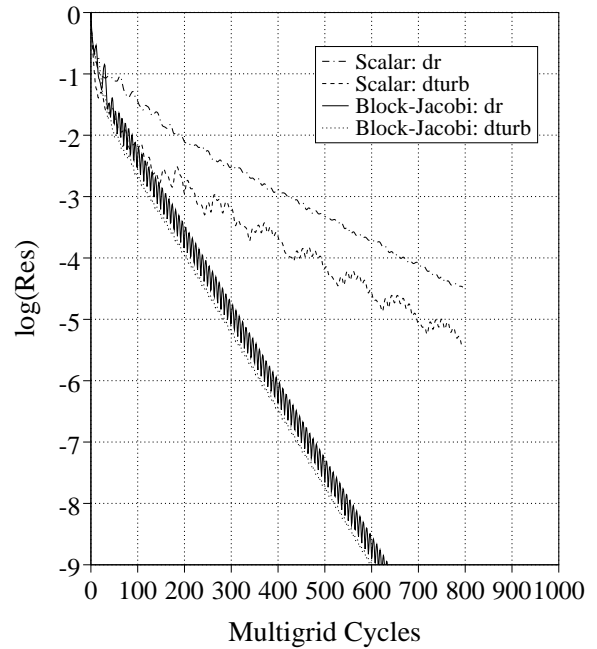


7d:  $C_D$  Convergence.

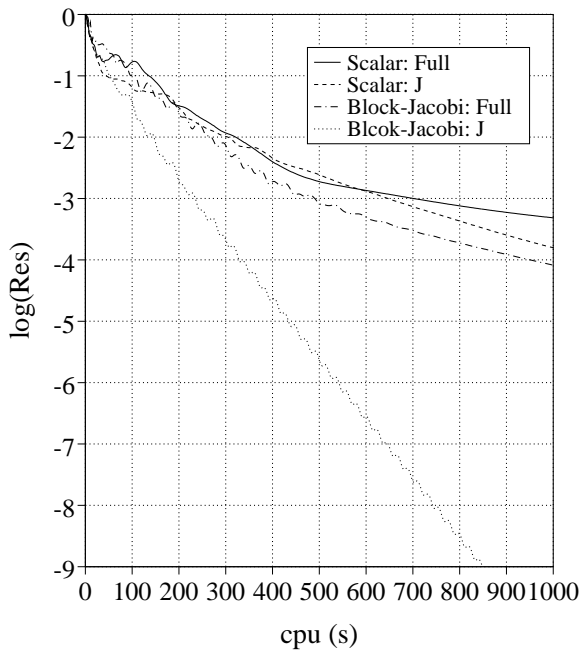
Figure 7: Flat Plate.  $M_\infty = 0.15$ ,  $\alpha = 0.0^\circ$ ,  $Re_L = 1 \times 10^5$ ,  $128 \times 32$  H-mesh. Matrix Switched Scheme.



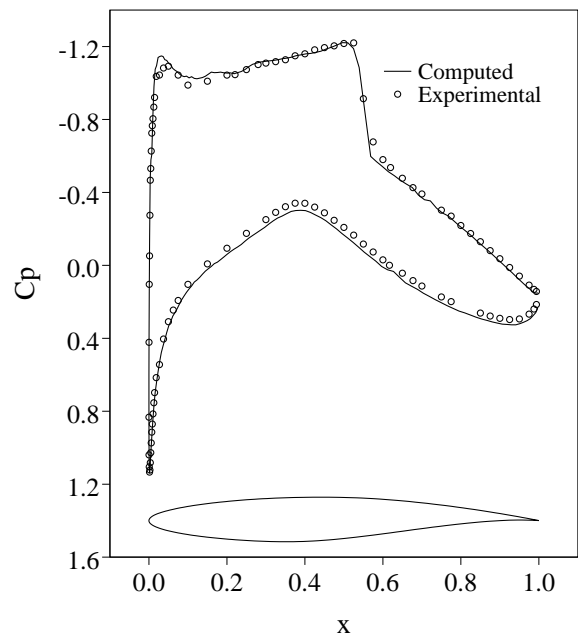
8a: Convergence.  
Full Coarsened Multigrid.



8b: Convergence.  
J-Coarsened Multigrid.

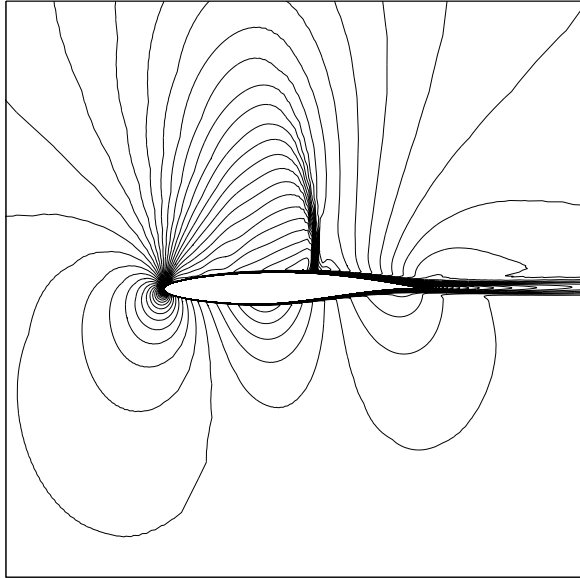


8c: Cost Comparison  
based on Density Residuals.

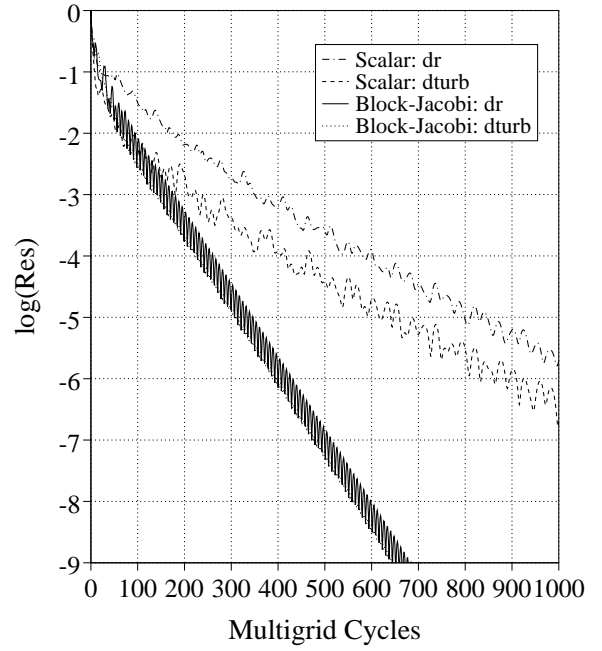


8d:  $C_p$ .  
 $C_l = .7757, C_d = .0142$

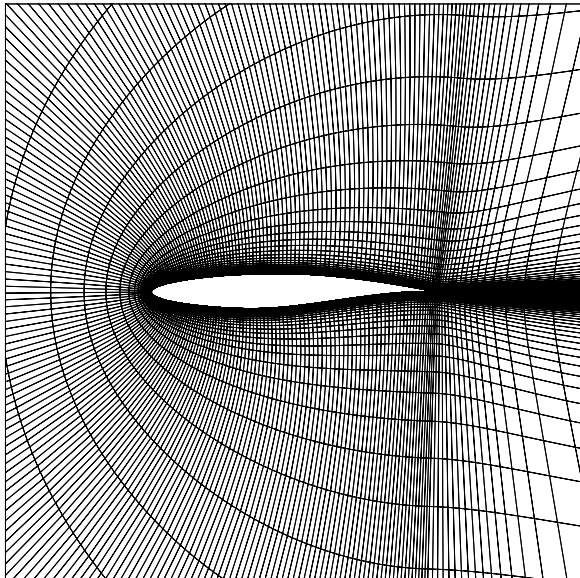
Figure 8: RAE2822 Airfoil. Case 6:  $M_\infty = 0.725, \alpha = 2.4^\circ, Re_L = 6.5 \times 10^6, 256 \times 64$  C-mesh.  
SA turbulence model with transition fixed at  $\frac{x}{L} = 0.03$ .



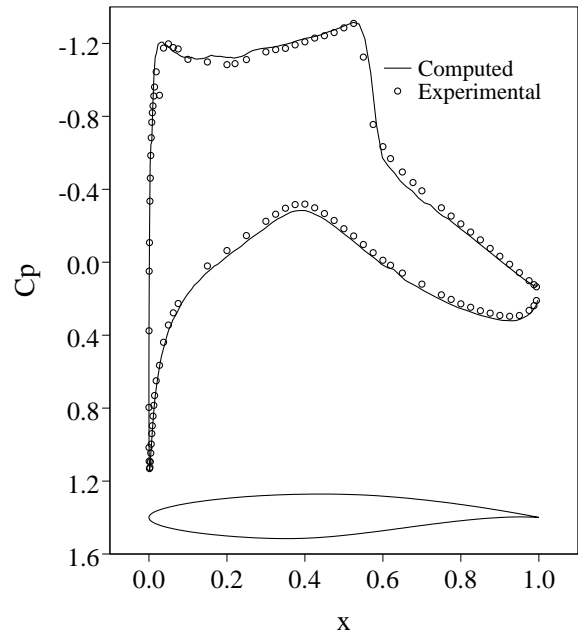
9a: Mach Number Contours.



9b: Convergence.



9c: Mesh.



9d:  $C_p$ .  
 $C_l = .8388, C_d = .0197$

Figure 9: RAE2822 Airfoil. Case 9:  $M_\infty = 0.73, \alpha = 2.79^\circ, Re_L = 6.5 \times 10^6$ ,  $256 \times 64$  C-mesh. SA turbulence model with transition fixed at  $\frac{x}{L} = 0.03$ .